Highly lithiophilic $Ti_3C_2T_x$-Mxene anchored on a flexible carbon foam scaffold as the basis for a dendrite-free lithium metal anode

TAO Fang-yu[1], XIE Dan[1], DIAO Wan-yue[1], LIU Chang[1], SUN Hai-zhu[1], LI Wen-liang[1,*], ZHANG Jing-ping[1,*], WU Xing-long[1,2,*]

（1. *Faculty of Chemistry*, *National & Local United Engineering Lab for Power Battery*, *Northeast Normal University*, *Changchun*, *Jilin* 130024, *China*; 2. *MOE Key Laboratory for UV Light-Emitting Materials and Technology*, *Northeast Normal University*, *Changchun*, *Jilin* 130024, *China*）

Abstract: We report the fabrication of a lithiophilic $Ti_3C_2T_x$ MXene-modified carbon foam ($Ti_3C_2T_x$-MX@CF) for the production of highly-stable LMBs that regulates Li nucleation behavior and reduces the volume change of a lithium metal anode (LMA). The 3D CF skeleton with a high specific surface area not only reduces the local current density to avoiding concentrated polarization, but also provides enough space to absorb the volume expansion during cycling. The excellent lithiophilicity of $Ti_3C_2T_x$-MX produced by its abundant functional groups reduces the Li nucleation overpotential, guides uniform Li deposition without the formation of Li dendrites, and maintains a stable SEI on the anode surface. Consequently, a Li infiltrated $Ti_3C_2T_x$-MX@CF symmetrical cell has an excellent cycling stability for more than 2 400 h with a low overpotential of 9 mV at a current density of 4 mA cm^{-2} and has a capacity of 1 mA h cm^{-2}. Furthermore, a Li- $Ti_3C_2T_x$-MX@CF||NCM111 full cell has a capacity of 129.6 mA h g^{-1} even after 330 cycles at 1 C, demonstrating the advantage of this method in constructing stable LMAs.

Key words: MXene; Three-dimensional structure; Dendrite suppression; Li metal anode

1 Introduction

Lithium metal batteries (LMBs) have been the subject of great research efforts due to the fascinating advantages of metallic Li, which include the lowest redox potential (−3.04 V *vs*. the standard hydrogen electrode) and the highest gravimetric theoretical capacity (3 860 mAh g^{-1})[1–4]. Unfortunately, the uncontrollable Li dendrite growth and infinite volume change during Li deposition/stripping processes have greatly hindered the practical application of LMBs[5–7]. The dendritic growths caused by the uneven Li^+ flux, easily pierce the separator and cause battery failure, often posing serious threats to safety[8–9]. The huge volume fluctuation is closely related to the inherent "hostless" property of metallic Li, which causes the solid electrolyte interface (SEI) film of lithium metal anodes (LMAs) to fracture, thereby inducing the reconstruction of SEI film, lowering the reversibility and limiting cycle lifespan of LMAs[10].

Recently, various strategies have been proposed to solve the above-mentioned problems, mainly including the optimization of electrolyte component[11–13], construction of a stable artificial interfacial layer on the surface of LMAs[14–15], and rational design of solid-state electrolyte[16–18]. Although modification of SEI film is able to enhance the stability of LMAs and improve electrochemical performance of LMBs to some extent, infinite volume expansion of LMAs arising from the "hostless" nature remains unresolved[19–20]. To this end, constructing a three-dimensional (3D) host has been viewed as the one of the most promising methods to resolve this issue[21]. This is attributed to the elaborately designed 3D skeleton (such as Cu, Ni and carbon foams) with high specific surface area and sufficient space, which not only lowers the local current density for homogenizing the distribution of Li^+ flux, but also accommodates the deposited Li metal for alleviating volume variations during repeated cycling[22–25]. Among them, accommodat-

Received date: 2023-02-20; **Revised date:** 2023-04-10

Corresponding author: LI Wen-liang, Professor. E-mail: liwl926@nenu.edu.cn;
ZHANG Jing-ping, Professor. E-mail: jpzhang@nenu.edu.cn;
WU Xing-long, Professor. E-mail: xinglong@nenu.edu.cn

Author introduction: TAO Fang-yu, Ph.D. E-mail: taofy704@nenu.edu.cn

Supplementary data associated with this article can be found in the online version.

ing deposited metallic Li into the 3D carbon skeleton with high electronic conductivity, flexibility and lightweight, is an attractive option[26]. The 3D carbon skeleton promotes fast Li deposition kinetics and guarantees high energy density of battery[27]. However, ordinary 3D carbon skeleton have a poor affinity for Li metal, which can result in high nucleation overpotential, triggering uneven Li deposition and Li dendrites growth[6]. Therefore, it is necessary to introduce lithiophilic materials into the 3D carbon skeleton to improve the overall lithiophilicity and facilitate uniform Li nucleation and growth[28].

It is well-accepted that introducing inorganic compounds with abundant functional groups can significantly improve the lithiophilicity of 3D carbon skeleton because of their strong interaction with metallic Li. For instance, two-dimensional (2D) transition metal carbides, nitrides and carbonitrides, also known as MXenes, inherently possess abundant functional groups, high electrical conductivity and low ion diffusion barrier, and have been confirmed to convert the 3D carbon skeleton from the lithiophobic to lithiophilic, thereby inhibiting Li dendrites growth[29–32]. More interestingly, MXenes, as a typical 2D layered material, can form lightweight freestanding film through self-assembly method[33–34]. Unfortunately, the formed freestanding MXene film is composed of densely compacted nanosheets with limited space, that is fragile and can hardly withstand the volume change during Li deposition/stripping processes, inevitably leading to the battery failures. Consequently, it is of great significance to integrate the advantages of 3D carbon skeleton and MXenes to construct a 3D lithiophilic host for mitigating volume change and simultaneously guiding uniform Li deposition for realizing highly-stable and dendrite-free LMAs.

Herein, a lithiophilic $Ti_3C_2T_x$-MXene decorated carbon foam ($Ti_3C_2T_x$-MX@CF) is prepared *via* a simple wetting process for constructing stable and dendrite-free LMAs. In this structure, the obtained $Ti_3C_2T_x$-MX@CF anode presents several advantages: (1) Thanks to their good affinity with metallic Li, —O and —F groups of $Ti_3C_2T_x$-MX can serve as nucleation sites to guide the homogeneous Li nucleation and growth, thus suppressing the formation of Li dendrites. (2) The 3D $Ti_3C_2T_x$-MX@CF skeleton possesses a large specific surface area, which decreases the local current density and ensures uniform Li^+ flux. (3) The 3D $Ti_3C_2T_x$-MX@CF framework consisting of interconnected networks provides enough space for accommodating deposited Li and mitigating volume fluctuation of LMAs during the repeated cycling. As a result, the $Ti_3C_2T_x$-MX@CF-based symmetrical cell achieves a long cycling life up to 2 400 h at a high current density of 4 mA cm^{-2} with an areal capacity of 1 mAh cm^{-2}. Meanwhile, under the higher areal deposition capacity of 10 mAh cm^{-2}, the $Ti_3C_2T_x$-MX@CF symmetrical cell still realizes stable cycling for more than 2 000 h. Upon pairing Li-$Ti_3C_2T_x$-MX@CF with $LiNiCoMnO_2$, the assembled full batteries show improved cycling and rate performance, indicating the potential of $Ti_3C_2T_x$-MX@CF in constructing high-performance LMBs.

2 Experimental

2.1 Fabrication of $Ti_3C_2T_x$-MX

$Ti_3C_2T_x$-MX was synthesized based on previous reports[30]. First, 2 g of LiF was added to 40 mL of 9 mol L^{-1} HCl solution, followed by stirring for 30 min. Then, 2 g Ti_3AlC_2 powder was slowly added into the above solution and stirred for 24 h at room temperature. Subsequently, the acidic mixture was repeatedly washed with deionized water and centrifuged at 8 000 r min^{-1} until the pH was ≈ 7. Then, the resulting solution was sonicated for 3 h. Finally, the suspension was poured out and centrifuged at 3 500 r min^{-1} for 5 min to obtain a dark green supernatant (7 mg mL^{-1}).

2.2 Fabrication of CF

The CF was obtained through one-step carbonization of the discarded facial mask tissue at 500 °C for 4 h under the Ar atmosphere.

2.3 Fabrication of $Ti_3C_2T_x$-MX@CF

The discarded facial mask tissue was first cut into desirable shapes and sizes, and then the $Ti_3C_2T_x$-MX was added to it dropwise. The obtained compos-

ite material was then dried overnight in an oven, and the $Ti_3C_2T_x$-MX@CF mixture was obtained by carbonization at 500 °C for 4 h in an Ar atmosphere.

2.4 Materials characterization

The morphology and crystal structures of materials were characterized by scanning electron microscopy (SEM, XL 30 ESEM-FEG, FEI Co.) and X-ray diffraction (XRD) patterns using a Rigaku P/max 2200VPC diffractometer with Cu *K*α radiation. The element mapping of samples was performed by using the EDX module equipped with the SEM.

To observe the surface morphology evolution of the electrodes during the Li plating/stripping process, the coin CR2032 cells were disassembled and washed using 1,2-dimethoxyethane (DME, Sigma-Aldrich, 99.8%) several times to remove the electrolyte in an argon-filled glove box with concentrations of H_2O and O_2 below 0.1×10^{-7}. Subsequently, the samples were quickly transferred to the vacuum chamber for SEM testing.

2.5 Electrochemical measurement

All the coin cells were assembled in an argon-filled glovebox. The galvanostatic charge-discharge experiments were carried out using the Neware battery testing system at room temperature. For half cells, Li||$Ti_3C_2T_x$-MX@CF and Li||CF cells were assembled with Li foil as the counter electrode, and $Ti_3C_2T_x$-MX@CF or CF electrode as the working electrode to investigate the reversibility of Li plating/stripping. Half cells were tested at 0.5 mA cm^{-2} with the plating capacity of 0.5 mAh cm^{-2} and 1 mAh cm^{-2} at 1 mA cm^{-2}. For symmetrical cells, Li foil and $Ti_3C_2T_x$-MX@CF or CF electrode as counter electrode and working electrode to assemble a symmetrical cell, and then 10 mAh cm^{-2} of Li was electrodeposited onto the $Ti_3C_2T_x$-MX@CF or CF electrode at a current density of 0.5 mA cm^{-2}. The cycling stability of symmetrical cells was studied at a fixed current density of 4 mA cm^{-2} and a capacity of 1 or 10 mA h cm^{-2}. Glass microfiber filter film was used as the separator and the 100 μL ether mixture consisting of 1 mol L^{-1} LiTFSI (Malklin, 99%) solution in 1∶1 (*v*/*v*) DOL (SigmaAldrich, 99%) and DME (Sigma-Aldrich, 99.8%) with 0.5 mol L^{-1} $LiNO_3$ (Aladdin, 99%) was used as the electrolyte. For full cells, the cathode electrode was fabricated by coating the cathode slurry (composed of $LiNiCoMnO_2$ (NCM111) powder∶PVDF∶super P = 7∶2∶1 using N-methyl-2-pyrrolidone (NMP) as the solvent) on Al foil and then drying in vacuum overnight at 100 °C. The loading amount of the NCM111 electrode was about 1.0-1.2 mg cm^{-2}. The 1 mol L^{-1} $LiPF_6$ in EC/DEC (*v*/*v* = 1/1) was used as the electrolyte. The pre-cycled anode was obtained by disassembling cells to get working electrodes that had been deposited 5 mA h cm^{-2} Li on $Ti_3C_2T_x$-MX@CF or CF. The cycle life and rate performance of full cells were tested by galvanostatic charge/discharge at 1 C and 5 C (1 C = 150 mAh g^{-1}) and the voltage window was set to 2.0-4.3 V.

3 Results and discussion

3.1 Characterization of $Ti_3C_2T_x$-MX@CF

The $Ti_3C_2T_x$-MX was successfully fabricated through a convenient acid etching method. As displayed in Fig. S1a and 1b, Ti_3AlC_2 precursor presents a typical layered structure with a large number of small irregular granules, while $Ti_3C_2T_x$-MX shows an obvious multilayer structure with expanded interlayer spacing after selectively etching the Al layers (Fig. S1c and 1d). The corresponding X-ray diffraction (XRD) patterns were employed to reflect the chemical composition changes before and after the etching process of the $Ti_3C_2T_x$-MX (Fig. 1d). As shown, the diffraction peak of (104) plane in $Ti_3C_2T_x$-MX disappeared, representing the successful etching of Al layers. Moreover, the characteristic peak of (002) plane shifts from 9.44° (Ti_3AlC_2) to 8.73° ($Ti_3C_2T_x$-MX) after etching, indicating the expansion of interlayer spacing and demonstrating the successful preparation of $Ti_3C_2T_x$-MX. Subsequently, $Ti_3C_2T_x$-MX suspension was added dropwise on the surface of non-woven fabric composed of parallelly aligned fibers (Fig. 1a and Fig. S2a) and then subjected to annealing in a furnace to prepare the $Ti_3C_2T_x$-MX@CF. As demonstrated, MXene was firmly and uniformly coated on the CF after the full infiltration

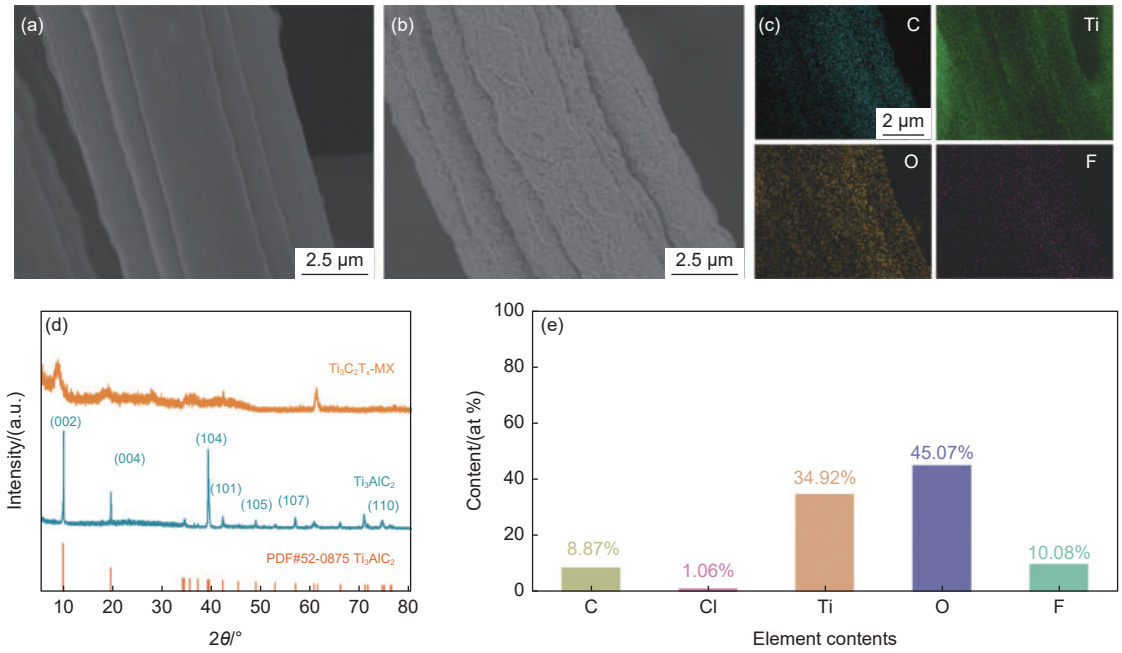

Fig. 1 SEM images of (a) bare CF and (b) $Ti_3C_2T_x$-MX@CF. (c) Elemental mapping of $Ti_3C_2T_x$-MX@CF. (d) XRD of Ti_3AlC_2 precursor and $Ti_3C_2T_x$-MX. (e) Element contents obtained by XRD measurement in $Ti_3C_2T_x$-MX@CF

and carbonization without any aggregation (Fig. 1b and Fig. S2b). The corresponding energy dispersive X-ray spectrometer (EDS) elemental mapping characterization indicates the uniform distribution of C, Ti, O and F elements on the CF surface and the content of elements is 8.87%, 35.92%, 45.97% and 10.08%, respectively, which can provide enough nucleation sites and effectively reduce the nucleation overpotential of metallic Li through strong interaction between metallic Li and heteroatoms (Fig. 1c and e).

3.2 Electrochemical behaviors of $Ti_3C_2T_x$-MX@CF

To investigate the effect of the $Ti_3C_2T_x$-MX@CF composites on the Li deposition/stripping behavior and constructing dendrite-free LMAs, the surface morphology evolution and thickness change of the CF and $Ti_3C_2T_x$-MX@CF electrode was observed via ex-situ SEM and cross-section images at 0.5 mA cm^{-2} with various Li plating/stripping capacities. Fig. 2a shows the plating and stripping voltage profile of the $Ti_3C_2T_x$-MX@CF electrode. As shown in Fig. 2b and 2c, when deposition capacity is 2 mAh cm^{-2}, Li metal is uniformly nucleated and grown on the wrinkled $Ti_3C_2T_x$-MX of CF surface benefited from the strong Li affinity of $Ti_3C_2T_x$-MX. Meanwhile, the thickness of $Ti_3C_2T_x$-MX@CF electrode exhibits a negligible change in comparison to that of the original state (255.65 *vs*. 255.25 μm, Fig. S4a and Fig. 5a), suggesting that the Li deposition process tends to start from the lithiophilic $Ti_3C_2T_x$-MX@CF surface. As the plating capacity increases to 4 and 6 mAh cm^{-2}, the $Ti_3C_2T_x$-MX is fully wrapped with deposited Li, and the edges of $Ti_3C_2T_x$-MX@CF become plump (Fig. 2d-g). However, the $Ti_3C_2T_x$-MX@CF surface always remains flat without the formation of Li dendrites during the entire Li deposition processes, demonstrating that the introduction of $Ti_3C_2T_x$-MX can offer numerous lithiophilic sites to guide homogeneous Li deposition. Moreover, the thickness of the $Ti_3C_2T_x$-MX@CF electrode varies from 256.70 to 257.49 μm, meaning that the $Ti_3C_2T_x$-MX@CF with interconnected fiber structure provides enough space for accommodating the deposited Li metal. During the subsequent charging process, the parallel-aligned $Ti_3C_2T_x$-MX@CF architecture gradually becomes clear and the wrinkled $Ti_3C_2T_x$-MX reemerges (Fig. 2h-m). It is worth noting that the surface of the $Ti_3C_2T_x$-MX@CF skeleton is smooth without residual Li metal, and the thickness of the electrode is close to the initial state after charging to 0.5 V (Fig. S4f), fur-

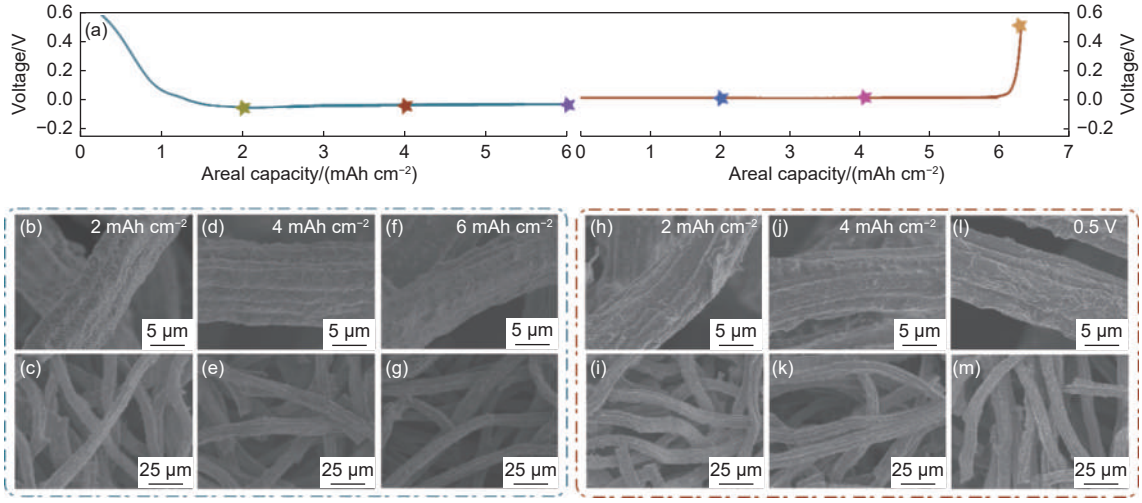

Fig. 2　(a) Voltage profile of the $Ti_3C_2T_x$-MX@CF electrode at a current density of 0.5 mA cm^{-2} and capacity of 6 mAh cm^{-2}. Morphology evolution of the $Ti_3C_2T_x$-MX@CF electrodes during the initial cycle of the Li plating/stripping process: After the anode was plated with (b, c) 1 mAh cm^{-2}, (d, e) 2 mAh cm^{-2}, and (f, g) 5 mAh cm^{-2} of Li metal; after stripping Li of (h, i) 2 mAh cm^{-2}, (j, k) 4 mAh cm^{-2} and (l, m) charged to 0.5 V from the $Ti_3C_2T_x$-MX@CF anode

ther demonstrating the effectiveness of the $Ti_3C_2T_x$-MX@CF in suppressing Li dendrites and alleviating the volume change during the Li plating/stripping processes. As for the CF, owing to the interconnected network of CF accommodating the deposited metal Li and buffering the volume change to some extent, the thickness of the CF electrode was slightly increased from 254.64 to 258.10 μm (Fig. S4g-i). Nevertheless, the deposited Li metal on the CF surface tends to aggregate into large chunks and then grows into filamentary Li dendrites due to the lack of nucleation sites on the CF surface (Fig. S3a-f). After the Li was stripped, a large number of the "dead Li" and dendritic Li is left behind the surface of the bare CF skeleton (Fig. S3g-l and Fig. S4l). These results indicate that $Ti_3C_2T_x$-MX@CF can be expected to improve the reversibility of LMAs and realize highly-stable LMBs.

Symmetric cells were assembled to evaluate the stability of Li-$Ti_3C_2T_x$-MX@CF during long-term cycling. Initially, 5 mAh cm^{-2} of Li is deposited onto the $Ti_3C_2T_x$-MX@CF to construct the Li-$Ti_3C_2T_x$-MX@CF electrode. Meanwhile, 5 mAh cm^{-2} of Li is pre-deposited onto the CF for comparison. As shown in Fig. 3a, the symmetric Li-$Ti_3C_2T_x$-MX@CF cell presents a steady voltage hysteresis with a low overpotential of 9 mV after 2 400 h at 4 mA cm^{-2} with an areal capacity of 1 mAh cm^{-2}. On the contrary, the voltage hysteresis of the symmetric Li-CF cell show obvious fluctuations and sudden increases in voltages caused by the dendrite growth and accumulation of "dead Li", indicating the failure of the cells. This result is further verified in the voltage hysteresis of Li charge/discharge with Li-$Ti_3C_2T_x$-MX@CF and Li-CF electrodes (Fig. 3b). When the Li deposition capacity increased to 10 mAh cm^{-2} (Fig. 3c), the Li-$Ti_3C_2T_x$-MX@CF electrode continued to show stable cycle for 2 200 h with low overpotential of 22 mV. In sharp contrast, the symmetric battery with Li-CF presents a drastic voltage fluctuation and the overpotential increases to 2 V after 88 h. Besides, Table S1 compares the cycling performance of $Ti_3C_2T_x$-MX@CF with that of the previously reported LMAs based on 3D carbon frameworks. It is clearly seen that the $Ti_3C_2T_x$-MX@CF electrode exhibits superior cycling stability with the lowest voltage hysteresis, demonstrating its application potential for advanced dendrite-free LMAs. The significantly improved cycling performance of Li-$Ti_3C_2T_x$-MX@CF is mainly attributed to the $Ti_3C_2T_x$-MX@CF with enriched lithiophilic sites and high electronic conductivity lowering the nucleation overpotential and promoting Li deposition kinetics, thus directing uniform Li deposition behaviors and inhibiting Li dendrites formation. Subsequently, the morphology variation of the electrodes after cycling was observed by the *ex-situ* SEM images. As shown in Fig. S6a and S6b, bulk and loose "dead Li"

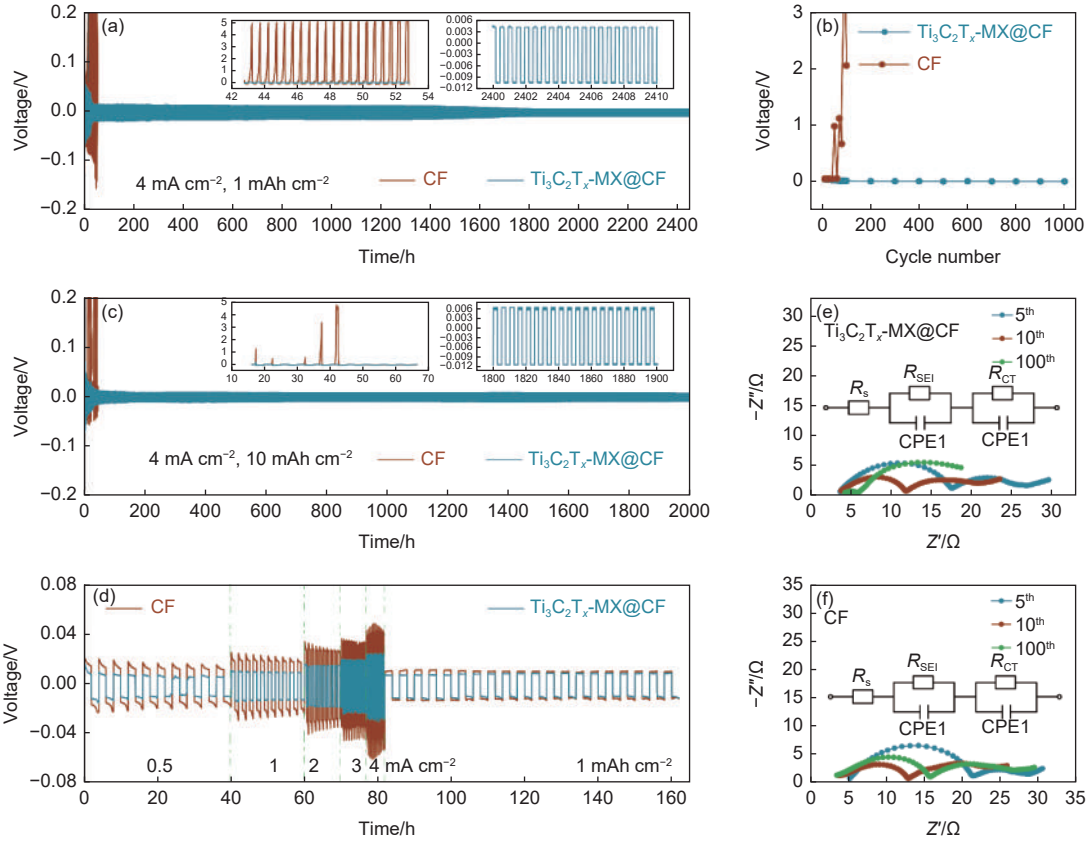

Fig. 3 Voltage profiles of Li-CF and Li-$Ti_3C_2T_x$-MX@CF electrodes in symmetric cells at (a) 4 mA cm^{-2} with a plating/stripping capacity of 1 mAh cm^{-2} and (b) the corresponding voltage hysteresis. (c) Voltage profile of Li-CF and Li-$Ti_3C_2T_x$-MX@CF symmetric cells under a large plating/stripping capacity of 10 mAh cm^{-2}. (d) Rate performances of Li-CF and Li-$Ti_3C_2T_x$-MX@CF symmetric cells. (e, f) Electrochemical impedance spectroscopy of Li-CF and Li-$Ti_3C_2T_x$-MX@CF symmetric cells at different cycles

with pores and cracks is accumulated on the surface of the CF. By contrast, a smooth and dendrite-free surface is observed in the $Ti_3C_2T_x$-MX@CF skeleton (Fig. S6c and d), implying that the $Ti_3C_2T_x$-MX@CF electrode induces uniform Li metal depositions and suppresses dendrites growth. Fig. 3d shows the rate performance of symmetric cells at various current densities ranging from 0.5 to 4 mA cm^{-2} at a constant capacity of 1 mAh cm^{-2}. With the current density increasing from 0.5 to 4 mA cm^{-2}, the Li-$Ti_3C_2T_x$-MX@CF symmetric cells deliver gradually elevated overpotential of 10, 14, 19, 24 and 28 mV respectively. However, the Li-CF symmetric cell shows much larger voltage hysteresis compared with Li-$Ti_3C_2T_x$-MX@CF, which is attributed to the lack of lithiophilic sites of CF. This causes the uneven nucleation of Li metal, thereby resulting in the generation of Li dendrites and “dead Li” during the long cycles. Impressively, when the current density changes back from 4 to 0.5 mA cm^{-2}, the overpotential of the Li-$Ti_3C_2T_x$-MX@CF still returns to 7 mV, indicating fast ion/electron transport kinetics and excellent structural stability of Li-$Ti_3C_2T_x$-MX@CF composite anode. The advantages of the Li-$Ti_3C_2T_x$-MX@CF anode in terms of interfacial stability were proven by electrochemical impedance spectroscopy (EIS) analysis. Fig. 3e and 3f display the Nyquist plots of the impedance spectra and the corresponding equivalent circuit diagram, and the simulated impedance parameters are listed in Table S2 (Supporting Information). It is observed that the R_{SEI} and R_{ct} of the Li-$Ti_3C_2T_x$-MX@CF cell gradually reduce within 100 cycles, implying a gradual stabilization process. Besides, the Li-$Ti_3C_2T_x$-MX@CF electrode shows lower SEI resistance (R_{SEI}) and charge transfer resistance (R_{ct}) compared with that of the Li-CF electrode at a different number of cycles, suggesting the formation of a stable SEI layer and improved charge-transfer kinetics in the $Ti_3C_2T_x$-

MX@CF host[35].

The coulombic efficiency (CE) is a crucial parameter for evaluating the sustainability of composite Li anode during the cycling processes, which is defined as the ratio of stripped capacity to plated capacity[36]. The CE was studied by assembling asymmetric cells with $Ti_3C_2T_x$-MX@CF and bare CF as the working electrodes and Li foil as the counter electrode in both cells. The CE of CF anode shows an obvious overcharge phenomenon after 110 cycles under a plating capacity of 0.5 mAh cm^{-2} at the current density of 0.5 mA cm^{-2}, which is the result of the reestablishment of electrical connection of "dead Li" during the following Li deposition processes[37]. By contrast, Li||$Ti_3C_2T_x$-MX@CF cell exhibits stable cycling over 120 cycles with a high average CE of 99.5% (Fig. 4a), benefiting from the $Ti_3C_2T_x$-MX@CF with abundant lithiophilic sites inducing a homogeneous Li deposition, maintaining a stable SEI layer, mitigating the volume change of LMAs during repeated cycling. As the deposition capacity increased to 1.0 mAh cm^{-2} with the same current density (Fig. 4b), the $Ti_3C_2T_x$-MX@CF continues to display a stable CE for more than 120 cycles with an average CE as high as 99.8%. In the case of CF, an obvious decline of CE is observed after merely 30 cycles resulting from uneven Li deposition and dendritic Li growth caused by the lithiophobic nature of CF. These results indicate that the $Ti_3C_2T_x$-MX decorated CF host can significantly enhance the reversibility during the Li plating/stripping process due to the excellent lithiophilicity of $Ti_3C_2T_x$-MX. Besides, Li||$Ti_3C_2T_x$-MX@CF cell ex-

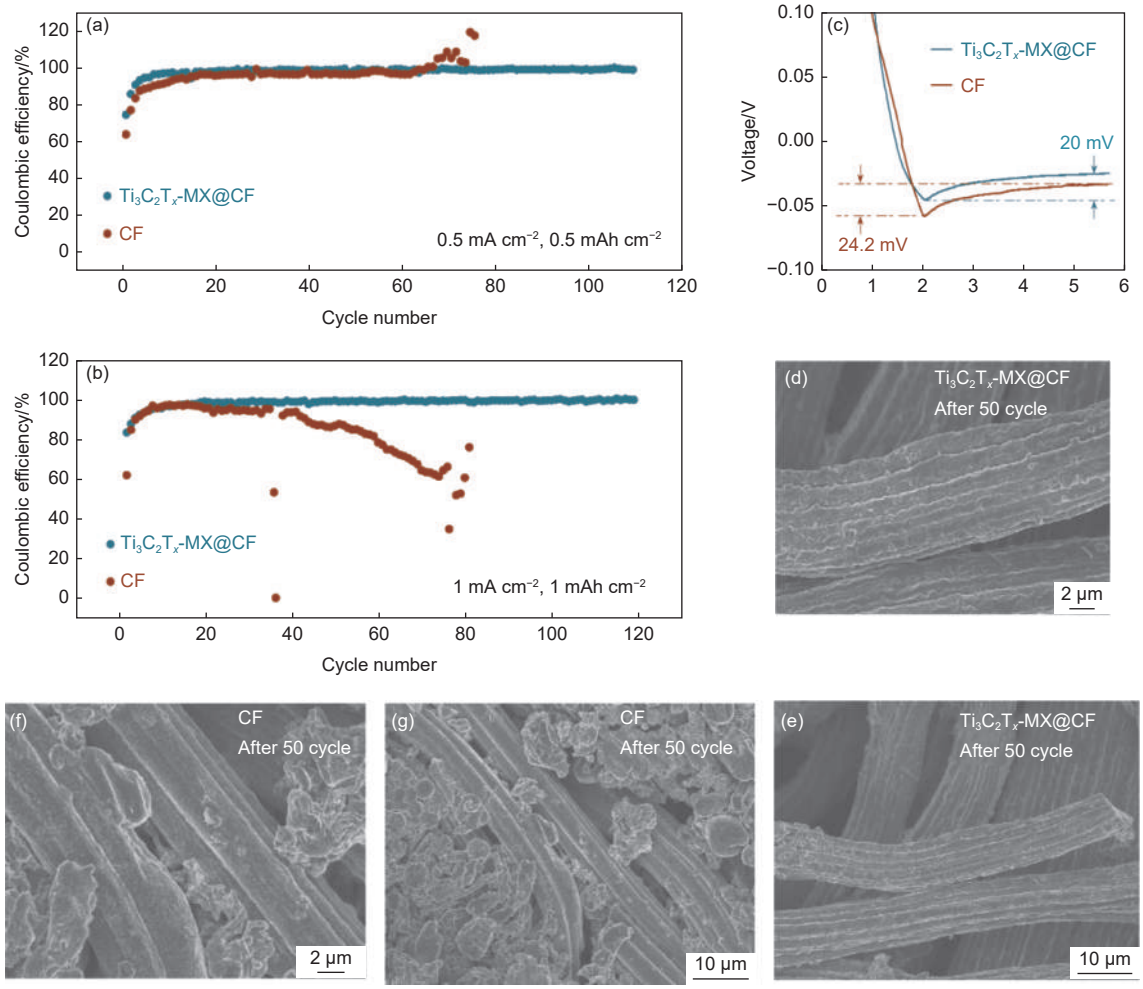

Fig. 4　Comparative coulombic efficiencies of Li plating/stripping on $Ti_3C_2T_x$-MX@CF and CF at (a) 0.5 mA cm^{-2}, 0.5 mAh cm^{-2} and (b) 1 mA cm^{-2}, 1 mAh cm^{-2}. (c) Nucleation overpotential of Li on the $Ti_3C_2T_x$-MX@CF and CF electrode. SEM images of (d, e) $Ti_3C_2T_x$-MX@CF and (g, e) CF electrode after the 50th cycle in the charge state

hibits a smaller nucleation overpotential (20 mV) at 0.5 mA cm^{-2} in comparison with Li||CF cells (24.2 mV), attributed to a large number of nucleation sites provided by $Ti_3C_2T_x$-MX which increase the affinity with Li and reduce the nucleation energy barrier (Fig. 4c). The surface morphology of Li plating/stripping for 50 cycles is displayed in Fig. 4d-g. Massive Li dendrites and "dead Li" are accumulated on the bare CF surface, while the $Ti_3C_2T_x$-MX@CF surface remains flat and smooth, further confirming the positive effect of designed $Ti_3C_2T_x$-MX@CF on inhibiting Li dendrites formation and enhancing the interfacial stability between electrode and electrolyte.

To demonstrate the feasibility of $Ti_3C_2T_x$-MX@CF in practical application of LMBs, 5 mAh cm^{-2} of Li metal was electrodeposited on $Ti_3C_2T_x$-MX@CF to fabricate the Li-$Ti_3C_2T_x$-MX@CF anode, and then matched with $LiNiCoMnO_2$ (NCM111) cathode to assemble the full cell. Fig. 5a shows the rate performance of Li-$Ti_3C_2T_x$-MX@CF||NCM111 and Li-CF||NCM111 full cell. As expected, the Li-$Ti_3C_2T_x$-MX@CF||NCM111 full cell exhibits the discharge capacities of 202.4, 186.2, 180.1, 174.8, 171.9, 162.2, 149.2, 141.1, 132.7 and 124.7 mAh g^{-1} at the current densities of 0.1, 0.2, 0.3, 0.4, 0.5, 1, 2, 3, 4 and 5 C, respectively. More interestingly, when the current density is switched back to 0.1 C, the discharge capacity of full cell remains close to the original value, indicative of the excellent reversibility of Li-$Ti_3C_2T_x$-MX@CF aided by $Ti_3C_2T_x$-MX. In contrast, the Li-CF||NCM111 full cell exhibits a relatively high discharge capacity before 0.5 C rate, but dropped sharply from 1 to 5 C due to the generation of Li dendrite growth and "dead Li". The long-term cycling stability of these batteries is tested at the current density of 1 C shown in Fig. 5b. As expected, the full

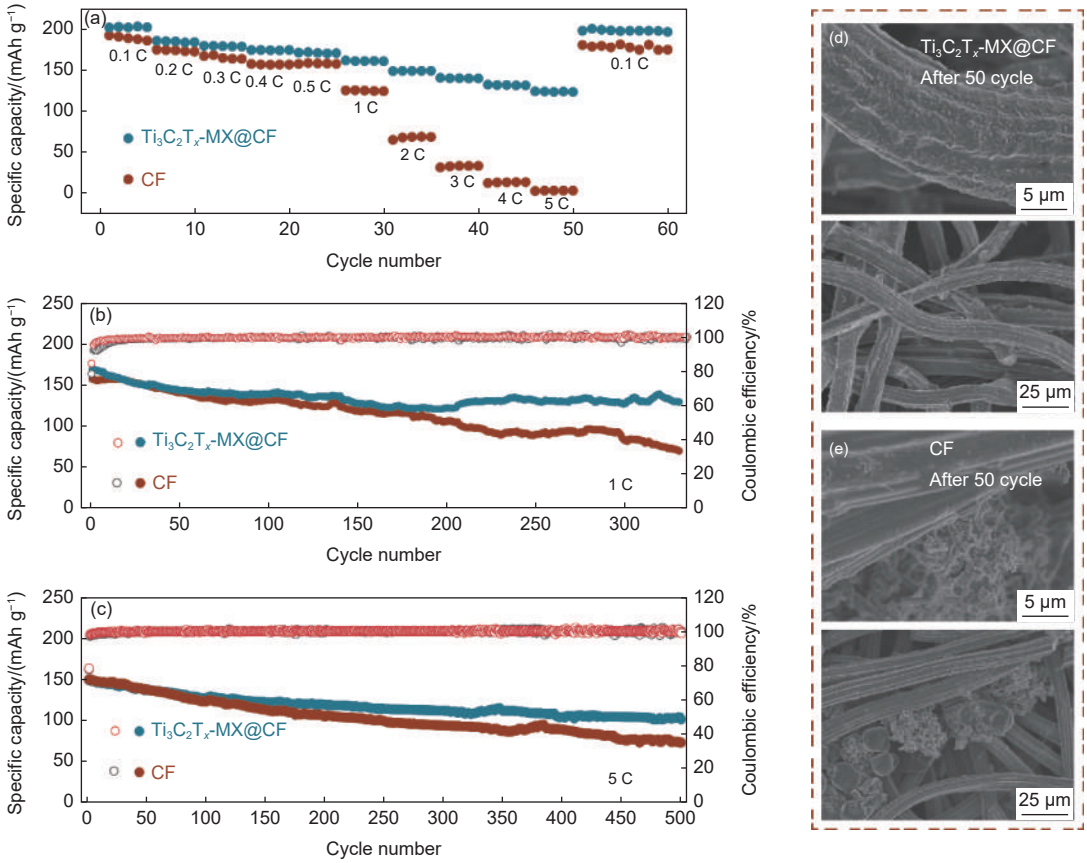

Fig. 5 (a) Rate performance of Li-$Ti_3C_2T_x$-MX@CF||NCM111 and Li-CF||NCM111 full cells at different current densities. Cycling performance of Li-$Ti_3C_2T_x$-MX@CF||NCM111 and Li-CF||NCM111 full cells at a current density of (b)1 C (1 C = 150 mAh g^{-1}) and (c) 5 C. The top-view SEM image of (d) Li-$Ti_3C_2T_x$-MX@CF anode and (e) Li-CF in the NCM111 full cell after 50 cycles at 1 C

cell assembled with the Li-$Ti_3C_2T_x$-MX@CF anode displays an initial specific capacity of 168.8 mAh g^{-1} and retains 129.6 mAh g^{-1} after 330 cycles (capacity retention of 76.8%). For Li-CF anode, an initial specific capacity of 157.5 mAh g^{-1} is obtained and delivers a capacity of 69.7 mAh g^{-1} after 330 cycles. Further elevating the current density to 5 C, the Li-$Ti_3C_2T_x$-MX@CF||NCM111 full cell still maintains a high discharge capacity of 101.5 mAh g^{-1} after cycling for 500 cycles, corresponding to an ultralow capacity fade of 0.14% per cycle, which is much better than that of Li-CF||NCM111 (discharge capacity of 73 mA h g^{-1} after 500 cycles, Fig. 5c). Moreover, it is clear from the *ex-situ* SEM images after 100 cycles (Fig. 5d and 5e) that the surface of bare CF accumulates Li dendrites and "dead Li", while the Li-$Ti_3C_2T_x$-MX@CF anode presents a smooth and clean surface without the formation of "dead Li" and Li dendrites. These results indicate that the Li anode modified with $Ti_3C_2T_x$-MX@CF can effectively suppress the growth of Li dendrites, maintain the integrity of the electrode structure, and alleviate the volume change of LMAs during the repeated cycling and will likely find practical applications in LMBs.

4 Conclusion

In summary, we have successfully constructed dendrite-free LMAs by using CF modified with lithiophilic $Ti_3C_2T_x$-MX as 3D host. The $Ti_3C_2T_x$-MX with abundant lithiophilic functional groups serves as nucleation sites to lower the Li nucleation barrier, and consequently induce uniform Li nucleation and suppress dendrite formation. Meanwhile, the 3D CF with interconnected network provides enough space for buffering the volume variation and lower the local current density through its high specific surface area, further inhibiting Li dendrite growth. Benefitting from the synergistic effect of lithiophilic $Ti_3C_2T_x$-MX and CF, a dendrite-free morphology is obtained and the assembled symmetrical cell displays excellent cycling stability up to 2 000 h at current density of 4 mA cm^{-2} with capacity of 10 mAh cm^{-2}. Moreover, the Li-$Ti_3C_2T_x$-MX@CF||NCM11full cells exhibit the improved cycling stability and rate performance. This work provides an instructive guidance for protecting LMAs and realizing high-performance LMBs.

Data availability statement

The data that support the findings of this study are openly available in Science Data Bank at https://www.doi.org/10.57760/sciencedb.j00125.00032 or https://resolve.pid21.cn/31253.11.sciencedb.j00125.00032.

Acknowledgements

This work was supported by the financial support from the Natural Science Foundation of Jilin Province (20220508141RC), the 111 Project (B13013), the National Natural Science Foundation of China (21873018), the Education Department of Jilin Province (JJKH20221154KJ), Jilin Provincial Research Center of Advanced Energy Materials (Northeast Normal University).

References

[1] Zhang N, Du L, Zhang J, et al. Self-assembled tent-like nanocavities for space-confined stable lithium metal anode[J]. Advanced Functional Materials, 2023, 33(16): 2210862.

[2] Yang Z, Liu W, Chen Q, et al. Ultra-smooth and dense lithium deposition toward high-performance lithium metal batteries[J]. Advanced Materials, 2023, 35(15): 2210130.

[3] Zhu H Y, Dong S Y, Xiong J, et al. MOF derived cobalt-nickel bimetallic phosphide (CoNiP) modified separator to enhance the polysulfide adsorption-catalysis for superior lithium-sulfur batteries[J], Journal of Colloid & Interface Science, 2023, 641: 942-949.

[4] Xu X, Li F, Zhang D, et al. Facile construction of CoSn/Co_3Sn_2@C nanocages as anode for superior lithium - /sodium - ion storage[J]. Carbon Neutralization, 2023, 2: 54-62.

[5] Li Y, Li J, Xiao H, et al. A novel 3D Li/Li_9Al_4/Li-Mg alloy anode for superior lithium metal batteries[J]. Advanced Functional Materials, 2023, 33(14): 2213905.

[6] Ye S, Chen X, Zhang R, et al. Revisiting the role of physical confinement and chemical regulation of 3D hosts for dendrite-free Li metal anode[J]. Nano-Micro Letters, 2022, 14(1): 187.

[7] Wang X, Huang R Q, Niu S Z, et al. Research progress on graphene-based materials for high-performance lithium-metal batteries[J]. New Carbon Materials, 2021, 36(4): 711-728.

[8] Zhang Y J, Wang H M, Liu X, et al. A dimensionally stable lithium

alloy based composite electrode for lithium metal batteries[J]. Chemical Engineering Journal, 2022, 450: 138074.

[9] Kong Z k, Chen Y, Hua J z, et al. Ultra-thin 2D MoO_2 nanosheets coupled with CNTs as efficient separator coating materials to promote the catalytic conversion of lithium polysulfides for advanced lithium-sulfur batteries[J]. New Carbon Materials, 2021, 36(4): 810-820.

[10] Zhan Y X, Shi P, Jin C B, et al. Regulating the two-stage accumulation mechanism of inactive lithium for practical composite lithium metal anodes[J]. Advanced Functional Materials, 2022, 32: 2206834.

[11] Qiao L, Oteo U, Martinez-Ibanez M, et al. Stable non-corrosive sulfonimide salt for 4-V-class lithium metal batteries[J]. Nature Materials, 2022, 21: 455-462.

[12] Yu Z, Rudnicki P E, Zhang Z, et al. Rational solvent molecule tuning for high-performance lithium metal battery electrolytes[J]. Nature Energy, 2022, 7(1): 94-106.

[13] Chen D, Liu Y, Xia C, et al. Polybenzimidazole functionalized electrolyte with Li - wetting and self - fluorination functionalities for practical Li metal batteries[J]. InfoMat, 2021, 4(5): e12247.

[14] Sun S, Myeong S, Kim J, et al. Design of inorganic/organic bi-layered Li protection layer enabled dendrite-free practical Li metal battery[J]. Chemical Engineering Journal, 2022, 450: 137993.

[15] Zhao J, Hong M, Ju Z, et al. Durable lithium metal anodes enabled by interfacial layers based on mechanically interlocked networks capable of energy dissipation[J]. Angewandte Chemie International Edition, 2022, 61: e202214386.

[16] Yao M, Ruan Q, Wang Y, et al. A robust dual-polymer@inorganic networks composite polymer electrolyte toward ultra-long-life and high-voltage Li/Li-rich metal battery[J]. Advanced Functional Materials, 2023, 33(18): 2213702.

[17] Li Z, Yu R, Weng S, et al. Tailoring polymer electrolyte ionic conductivity for production of low-temperature operating quasi-all-solid-state lithium metal batteries[J]. Nature Communications, 2023, 14: 482.

[18] Yang T Q, Wang C, Zhang W K, et al. Composite polymer electrolytes reinforced by a three-dimensional polyacrylonitrile/$Li_{0.33}La_{0.557}TiO_3$ nanofiber framework for room-temperature dendrite-free all-solid-state lithium metal battery[J]. Rare Metals, 2022, 41(6): 1870-1879.

[19] Abdul Ahad S, Bhattacharya S, Kilian S, et al. Lithiophilic nanowire guided Li deposition in Li metal batteries[J]. Small, 2023, 19: 2205142.

[20] Zhang S, Yang G, Li X, et al. Electrolyte and current collector designs for stable lithium metal anodes[J]. International Journal of Minerals, Metallurgy and Materials, 2022, 29(5): 953-964.

[21] Bao J, Pei H J, Yue X Y, et al. In situ formed synaptic Zn@LiZn host derived from ZnO nanofiber decorated Zn foam for dendrite-free lithium metal anode[J]. Nano Research, 2023, DOI: 10.1007/s12274-022-5089-5.

[22] Chen L, Chen G, Wen Z, et al. Electroplating CuO nanoneedle arrays on Ni foam as superior 3D scaffold for dendrite-free and stable Li metal anode[J]. Applied Surface Science, 2022, 599: 153955.

[23] Chen W, Li S, Wang C, et al. Targeted deposition in a lithiophilic silver-modified 3D Cu host for lithium-metal anodes[J]. Energy & Environmental Materials, 2023. DOI: 10.1002/eem2.12412.

[24] Li L X, Li Y N, Cao F F, et al. Lithiophilic interface guided transient infiltration of molten lithium for stable 3D composite lithium anodes[J]. Nano Research, 2023, 16: 8297-8303.

[25] Gao Y, Cui B F, Wang J J, et al. Improving Li reversibility in Li metal batteries through uniform dispersion of Ag nanoparticles on graphene[J]. Rare Metals, 2022, 41(10): 3391-3400.

[26] Zhang W, Fan Q, Zhang D, et al. Dynamic charge modulate lithium uniform plating functional composite anode for dendrite-free lithium metal batteries[J]. Nano Energy, 2022, 102: 107677.

[27] Zhang J, He R, Zhuang Q, et al. Tuning 4f-center electron structure by schottky defects for catalyzing Li diffusion to achieve long-term dendrite-free lithium metal battery[J]. Advanced Science, 2022, 9: 2202244.

[28] Yang Y, Cao J, Li W, et al. Ultrahigh-capacity and dendrite-free lithium metal anodes enabled by lithiophilic bimetallic oxides[J]. Journal of Materials Chemistry A, 2022, 10(44): 23896-23904.

[29] Zheng C, Yao Y, Rui X, et al. Functional MXene-based materials for next-generation rechargeable batteries[J]. Advanced Materials, 2022, 34: 2204988.

[30] Zhao F, Zhai P, Wei Y, et al. Constructing artificial SEI layer on lithiophilic MXene surface for high-performance lithium metal anodes[J]. Advanced Science, 2022, 9(6): 2103930.

[31] Zhao Y, Li Q, Liu Z, et al. Stable electrochemical Li plating/stripping behavior by anchoring MXene layers on three-dimensional conductive skeletons[J]. ACS Applied Materials & Interfaces, 2020, 12(34): 37967-37976.

[32] Wei C, Tao Y, An Y, et al. Recent advances of emerging 2D MXene for stable and dendrite-free metal anodes[J]. Advanced Functional Materials, 2020, 30(45): 2004613.

[33] Tan L, Wei C, Zhang Y, et al. Self-assembled, highly-lithiophilic and well-aligned biomass engineered MXene paper enables dendrite-free lithium metal anode in carbonate-based electrolyte[J]. Journal of Energy Chemistry, 2022, 69: 221-230.

[34] Qian Y, Wei C, Tian Y, et al. Constructing ultrafine lithiophilic layer on MXene paper by sputtering for stable and flexible 3D lithium metal anode[J]. Chemical Engineering Journal, 2021, 421: 129685.

[35] Liu Y, Sun C, Lu Y, et al. Lamellar-structured anodes based on lithiophilic gradient enable dendrite-free lithium metal batteries with high capacity loading and fast-charging capability[J]. Chemical Engineering Journal, 2023, 451: 138570.

[36] Zhou S, Fu C, Chang Z, et al. Conductivity gradient modulator induced highly reversible Li anodes in carbonate electrolytes for

high-voltage lithium-metal batteries[J]. Energy Storage Materials, 2022, 47: 482-490.

[37] Xie D, Li H H, Diao W Y, et al. Spatial confinement of vertical arrays of lithiophilic SnS_2 nanosheets enables conformal Li nucleation/growth towards dendrite-free Li metal anode[J]. Energy Storage Materials, 2021, 36: 504-513.